

Clouds form on the hot Saturn JWST ERO target WASP-96b

D. Samra¹ , Ch. Helling^{1,2}, K. L. Chubb³, M. Min⁴, L. Carone¹, and A. D. Schneider^{5,6}

¹ Space Research Institute, Austrian Academy of Sciences, Schmiedlstrasse 6, 8042 Graz, Austria
e-mail: dominic.samra@oeaw.ac.at

² Institute for Theoretical Physics and Computational Physics, Graz University of Technology, Petersgasse 16 8010 Graz, Austria

³ Center for Exoplanet Science, University of St Andrews, St Andrews KY16 9AJ, UK

⁴ SRON Netherlands Institute for Space Research, Niels Bohrweg 4, 2333 CA Leiden, The Netherlands

⁵ Institute of Astronomy, KU Leuven, Celestijnenlaan 200D, 3001 Leuven, Belgium

⁶ Center for ExoLife Sciences, Niels Bohr Institute, Øster Voldgade 5, 1350 Copenhagen, Denmark

Received 9 September 2022 / Accepted 26 October 2022

ABSTRACT

Context. WASP-96b is a hot Saturn exoplanet, with an equilibrium temperature of ≈ 1300 K. This is well within the regime of thermodynamically expected extensive cloud formation. Prior observations with *Hubble*/WFC3, *Spitzer*/IRAC, and VLT/FORS2 have been combined into a single spectrum for which retrievals suggest a cold but cloud-free atmosphere. Recently, the planet was observed with the *James Webb* Space Telescope (JWST) as part of the Early Release Observations (ERO).

Aims. The formation of clouds in the atmosphere of exoplanet WASP-96b is explored.

Methods. One-dimensional profiles were extracted from the 3D GCM expeRT/MITgcm results and used as input for a kinetic, non-equilibrium model to study the formation of mineral cloud particles of mixed composition. The ARCIS retrieval framework was applied to the pre-JWST WASP-96b transit spectrum to investigate the apparent contradiction between cloudy models and assumed cloud-free transit spectrum.

Results. Clouds are predicted to be ubiquitous throughout the atmosphere of WASP-96b. Silicate materials contribute between 40% and 90% cloud particle volume, which means that metal oxides also contribute with up to 40% cloud particle volume in the low-pressure regimes that affect spectra. We explore how these cloudy models match currently available transit spectra. Reduced vertical mixing acts to settle clouds to deeper in the atmosphere, and an increased cloud particle porosity reduces the opacity of clouds in the near-IR and optical region. These two effects allow for clearer molecular features to be observed while still allowing clouds to be in the atmosphere.

Conclusions. The atmosphere of WASP-96b is unlikely to be cloud free. Retrievals of HST, *Spitzer*, and VLT spectra also show that multiple cloudy solutions reproduce the data. JWST observations will be affected by clouds, where the cloud top pressure varies by an order of magnitude within even the NIRISS wavelength range. The long-wavelength end of NIRSpec and the short-wavelength end of MIRI may probe atmospheric asymmetries between the limbs of the terminator on WASP-96b.

Key words. planets and satellites: individual: WASP-96b – planets and satellites: atmospheres – planets and satellites: gaseous planets – planets and satellites: fundamental parameters

1. Introduction

The hot Saturn WASP-96b was one of the first¹ extrasolar planets for which *James Webb* Space Telescope (JWST) observations were released to the community on 12 July 2022. The primary transit of the planet was observed using the JWST NIRISS/SOSS² mode as part of the JWST early release observations (ERO; Pontoppidan et al. 2022). It therefore presents itself as a desirable target to analyse from a modelling perspective, in preparation for the newly reduced transit spectra that are expected to become available in the near future. WASP-96b has a mass of $0.48 \pm 0.03 M_{\text{Jup}}$, a mean radius of $1.2 \pm 0.06 R_{\text{Jup}}$, and orbits a G-type star in 3.4 days at a distance of 1120 lyr from Earth (Hellier et al. 2014). The orbit appears to be non-eccentric, and its global temperature is $T_{\text{glob}} \approx 1300$ K (1285 ± 40 , Hellier et al. 2014). Optical transmission spectra of WASP-96b have been observed pre-JWST by the FORS2 spectrograph on

the ground-based Very Large Telescope (VLT; Nikolov et al. 2018). The resolution of these VLT spectra allowed the Na doublet to be studied in detail; Na abundances were derived, and a cloud-free atmosphere was assumed because of broad Na I line wings (Nikolov et al. 2018). Nikolov et al. (2022) more recently used space-based instruments to observe further primary transits of WASP-96b, including the Infrared Array Camera (IRAC) on the *Spitzer* Space Telescope (*Spitzer*), and the Wide Field Camera 3 (WFC3) instrument on the *Hubble* Space Telescope (HST). These were combined with ground-based observations from the VLT for a more complete analysis of the planetary atmosphere. This is the set of observations that we use for some comparisons to our atmospheric models in this work. Nikolov et al. (2022) argued that their retrieval approach of these combined data suggests cloud- or haze-free terminators at the pressures probed by the observations. The retrieval procedure treats cloud particle rain-out and the element abundances for Na, K, C, and O as independent parameters. The authors derived solar-to-supersolar oxygen and sodium element abundances. A supersolar oxygen abundance may be the reason for the strong H₂O features that the authors presented as an additional reason to conclude that

¹ HAT-P-14b was observed during commissioning; this is strictly speaking the first exoplanet observation released in Rigby et al. (2022).

² Near Infrared Imager and Slitless Spectrograph/Single Object Slitless Spectroscopy.

the atmosphere of WASP-96b is cloud free. The metallicity derived for the host star WASP-96 is either solar or supersolar; [Hellier et al. \(2014\)](#) reported abundances compared to solar of 0.14 ± 0.19 dex, but more recent observations by [Nikolov et al. \(2022\)](#) suggested that WASP-96 has a higher metallicity.

A recently analysed observation of the brown dwarf VHS 1256-1257 b by [Miles et al. \(2022\)](#) using the JWST NIRSpec IFU³ and MIRI MRS⁴ modes revealed solid-state silicate features in the longer wavelength part of the atmospheric spectrum. This is strong evidence of small silicate particles in the atmosphere.

We demonstrate in this paper that mineral cloud particles that are made of a mix of metal-oxide and silicate components are expected to form in the atmosphere of the hot Saturn WASP-96b. We present a cloud map for this planet that demonstrates that it is completely covered with clouds. We identify WASP-96b as located at the boundary between the weather and climate regime for cool planets and the less homogeneous transition planets that were introduced in [Helling et al. \(2022\)](#). The absence of a strong morning and evening terminator asymmetry should improve the chances of observing spectral features of the ensemble of cloud particles that our microphysical models predict should populate the terminator regions.

2. Approach

We examined the cloud structure on the hot Saturn WASP-96b by adopting a hierarchical approach similar to works on the hot Jupiters HD 189733b and HD 209458b ([Lee et al. 2015](#); [Helling et al. 2016](#)) and the ultra-hot Jupiters WASP-18b ([Helling et al. 2019a](#)) and HAT-P-7b ([Helling et al. 2019b](#); [Molaverdikhani et al. 2020](#)): The first modelling step produced a cloud-free 3D General Circulation Model (GCM) result for a model representing WASP-96b. These results were used as input for the second modelling step, which was a kinetic cloud formation model consistently combined with equilibrium gas-chemistry calculations. We used 120 1D ($T_{\text{gas}}(z)$, $p_{\text{gas}}(z)$, $v_z(z)$)-profiles for WASP-96b similar to our previous works. $T_{\text{gas}}(z)$ is the local gas temperature [K], $p_{\text{gas}}(z)$ is the local gas pressure [bar], and $v_z(z)$ is the local vertical velocity component (cm s^{-1}).

This hierarchical approach has the limitation of not explicitly taking into account the potential effect of horizontal winds on cloud formation. However, processes governing the formation of mineral clouds are determined by local thermodynamic properties that are the result of 3D dynamic atmosphere simulations. Cloud particle properties such as particle size or particle composition could be somewhat smeared out in longitude compared to the results shown here. The temperature structure may change when the cloud particle opacity is fully taken into account in the solution of the radiative transfer. This may change the precise location of the cloud in pressure space, but not the principle result of clouds forming in WASP-96b.

3D atmosphere modelling. We used `expeRT/MITgcm` ([Carone et al. 2020](#); [Baeyens et al. 2021](#)) to model WASP-96b. `expeRT/MITgcm` builds on the dynamical core of `MITgcm` and has been adapted to model tidally locked gas giants. Recent extensions in [Schneider et al. \(2022\)](#) include non-grey radiative transfer coupling. The model parameters used for the GCM, representative of the hot Saturn WASP-96b, are $R_p = 8.58 \times 10^9$ cm, $P_{\text{rot}} = 3.4$ days, $\log_{10}(g [\text{cm s}^{-2}]) = 2.9$, and the substellar point

³ Near Infrared Spectrograph Integral Field Unit.

⁴ Mid-Infrared Instrument Medium Resolution Spectroscopy.

irradiation temperature $T_{\text{irr}} = 1819$ K (Table A.1). The model was run for 1400 days, and we note that the deepest layers may not be fully converged. A constant mean molecular weight of $\mu = 2.3$ was assumed for the 3D atmospheric modelling. This constant value is a reasonable assumption given that the thermodynamic structure of the atmosphere does not cause the gas composition to deviate from a H₂-dominated gas. Additional details for the 3D GCM setup can be found in Table A.1.

[Nikolov et al. \(2022\)](#) fit an isothermal blackbody to the dayside of WASP-96b using *Spitzer* observations, finding a dayside brightness temperature of 1545 ± 90 K. The equilibrium temperature of the planet can be calculated using $T_{\text{eq}} = \sqrt{R_{\star}/a_p} T_{\star} (f(1 - A_B))^{1/4}$, the final factor includes the heat redistribution factor (f) and the bond Albedo of the planet (A_B). Assuming full heat redistribution ($f = 1/4$) and full absorption of incident radiation ($A_B = 0$), we derived the equilibrium temperature of the planet: $T_{\text{eq}} = 1286$ K. As input to the initialisation of the GCM, the substellar irradiation temperature was used. This is the temperature of a blackbody reradiating the energy received from the star by the planet at the substellar point ($T_{\text{irr}} = 1819$ K, see Table A.1). Comparing these numbers to the observed brightness temperature is difficult. The brightness temperature sits between the planet equilibrium temperature and the substellar irradiation temperature. This indicates some level of heat redistribution around the planet, as well as the potential impact of cloud albedo. However, observations of similar temperature exoplanets have revealed low dayside albedos (e.g. [Schwartz & Cowan 2015](#); [Fraie et al. 2021](#); [Brandeker et al. 2022](#)).

Kinetic cloud formation. We applied the same kinetic cloud formation model (nucleation, growth, evaporation, gravitational settling, element consumption, and replenishment) and equilibrium gas-phase calculations as for our grid study in [Helling et al. \(2022\)](#). It is essential that the seed forming species are also considered as surface growth material, since both processes (nucleation and growth) compete for the participating elements (Ti, Si, O, Na, K, and Cl in this work). We considered the formation of 16 bulk materials ($s = \text{TiO}_2[s]$, $\text{Mg}_2\text{SiO}_4[s]$, $\text{MgSiO}_3[s]$, $\text{MgO}[s]$, $\text{SiO}[s]$, $\text{SiO}_2[s]$, $\text{Fe}[s]$, $\text{FeO}[s]$, $\text{FeS}[s]$, $\text{Fe}_2\text{O}_3[s]$, $\text{Fe}_2\text{SiO}_4[s]$, $\text{Al}_2\text{O}_3[s]$, $\text{CaTiO}_3[s]$, $\text{CaSiO}_3[s]$, and $\text{KCl}[s]$, $\text{NaCl}[s]$) that form from 11 elements (Mg, Si, Ti, O, Fe, Al, Ca, S, Na, K, and Cl) by 132 surface reactions. In total, we solved 31 ODEs to describe the formation of cloud condensation nuclei ($J_{\star}(z) = \sum_i J_i$, $i = \text{TiO}_2$, SiO , KCl , and NaCl) that grow to macroscopic sized cloud particles made of a mix of materials that changes depending on the local atmospheric gas temperature and gas pressure.

Retrieval and atmospheric spectra modelling with ARCIS. We followed the method of [Min et al. \(2020\)](#) by running a constrained retrieval on the previously published VLT/HST/*Spitzer* transmission spectra of WASP-96b (collated by [Nikolov et al. 2022](#)) using the Bayesian retrieval code `ARtful modelling Code for exoplanet Science (ARCIS)`. The constrained retrieval includes the cloud formation models of [Ormel & Min \(2019\)](#), with the variety of cloud species included in this work the same as in [Min et al. \(2020\)](#) with additional Na and K silicate clouds. It is a simplified approach in comparison to the previous hierarchical modelling stages of this work, but it enables us to compare some retrieved parameters to our kinetic cloud formation models, such as cloud particle size and expected cloud optical thickness.

It also allowed us to explore the effect on the spectra of some of these parameters, which we did using the forward-modelling mode of `ARCIS`. We generated simulated transmission

Table 1. Parameters and associated priors for the retrieval of WASP-96b VLT/HST/Spitzer data using ARCIS.

Name	Description	Priors
<i>Parameters included for both cloud formation and clear retrievals</i>		
R_p	Planet radius	5σ around lit. value ^(a) , units of R_J , flat linear prior
$\log_{10}(g_p)$	Base-10 logarithm of the planet surface gravity ^(b)	1 to 5 (with g given in cgs units)
C/O	Atmospheric carbon-to-oxygen ratio	0.1 (sub-solar) to 1.3 (super-solar), flat linear prior
N/O	Atmospheric nitrogen-to-oxygen ratio	0 (sub-solar) to 0.3 (super-solar), flat linear prior
Si/O	Atmospheric silicon-to-oxygen ratio	0 (sub-solar) to 0.3 (super-solar), flat linear prior
[Z]	Atmospheric metallicity (global)	-3 (sub-solar) to 3 (super-solar) dex, flat linear prior
$\log_{10}(\gamma)$	Ratio of visible to IR opacity	-2 to 2, flat log prior
f_{irr}	Irradiation parameter	0 to 0.25, flat linear prior
$\log_{10}(\kappa_{\text{IR}})$	Infrared opacity	-4 to 4 $\text{cm}^2 \text{g}^{-1}$, flat log prior
T_{int}	Temperature at an optical depth $\tau = \frac{2}{3}$ as caused by internal heat from the planet	10 to 3000 K, flat log prior
<i>Parameters included in cloud formation retrieval only</i>		
K_{zz}	Cloud diffusion coefficient	$10^5 - 10^{12} \text{ cm}^2 \text{ s}^{-1}$, flat log prior
$\log_{10} \dot{\Sigma}$	Nucleation rate	$10^{-17} - 10^{-7} \text{ g cm}^{-2} \text{ s}^{-1}$, flat log prior

Notes. A description of these parameters can be found in [Min et al. \(2020\)](#); [Chubb & Min \(2022\)](#). ^(a)[Hellier et al. \(2014\)](#). ^(b)We use a Gaussian prior on the mass based on radial velocity measurements of WASP-96b ([Hellier et al. 2014](#)). We compute the mass based on R_p and $\log(g_p)$ and then place the prior on this derived parameter.

spectra with varied atmospheric parameters that can be compared to observations. Here, we focus on the effects of clouds in the atmosphere and how they can be present, but still let us observe strong molecular features. The distribution of hollow spheres (DHS) method is employed in ARCIS to compute the cloud opacities ([Min et al. 2005](#)). This allows for the inclusion of non-spherical cloud particles and the ability to vary the porosity of the particles. A similar simple model for particle porosity that also incorporates the impacts of increased surface area and reduced settling on the clouds as well as optical effects was recently explored in [Samra et al. \(2020\)](#). We also explore the impact of this microphysically consistent model on the cloud optical depth in Sect. 3.4. The chemistry for all retrievals is constrained, with elemental abundances computed after the cloud formation process in order to take into account elements that may have formed into clouds. The equilibrium chemistry code GGChem⁵ ([Woitke et al. 2018](#)) was used to compute the molecular abundances given these elemental abundances. A summary of the retrieved parameters and their priors is given in Table 1. For comparison, we also ran a cloud-free retrieval, with all other parameters the same. We present the results of these retrievals in Sect. 4.1.

3. Cloud properties on the hot Saturn WASP-96b

3.1. 3D GCM atmosphere structure

The 3D GCM results for the hot Saturn WASP-96b suggest that a maximum day-to-night temperature contrast of $\approx 400\text{K}$ occurs in the low-pressure regimes at $p_{\text{gas}} < 10^{-2}$ bar. Figure 1 demonstrates this with the 120 1D profiles that were extracted from the 3D GCM solution. The morning terminator (dashed grey line) shows some moderate temperature inversion of $\approx 100\text{K}$ resulting from the cold gas being transported from the nightside to the dayside. The temperature differences between the morning and the evening terminators are $\approx 200\text{K}$ at most.

⁵ Short for Gleich-Gewichts-Chemie.

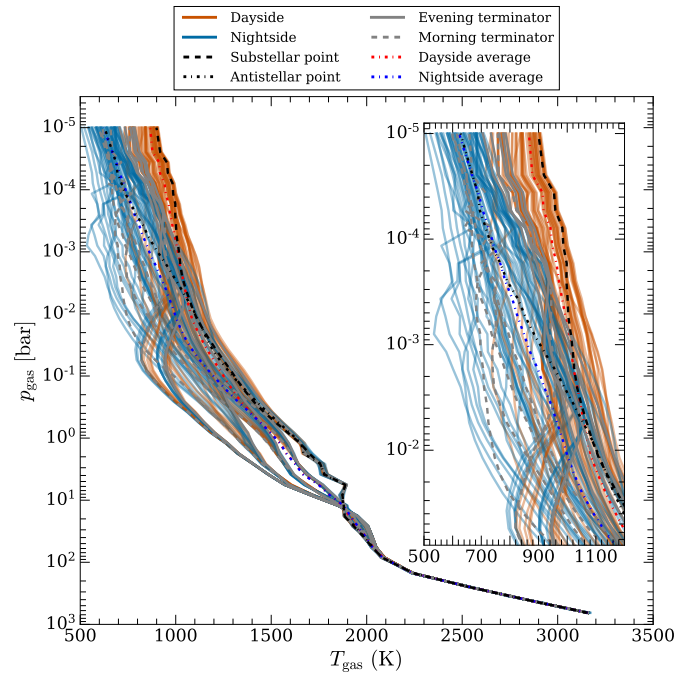


Fig. 1. Pressure-temperature structure of the 120 1D profiles extracted from the GCM results. Orange lines represent the dayside profiles, blue lines show the nightside profiles, and the grey lines show the terminator profiles. Dashed and dot-dashed black lines highlight the substellar and antistellar points respectively. Day- and nightside hemisphere averages are shown as dashed red and blue lines. The inset shows the upper atmosphere GCM of the profiles.

Based on its global temperature $T_{\text{glob}} \approx 1300\text{K}$, the hot Saturn WASP-96b falls on the boundary of the cool planet climate regime identified in [Helling et al. \(2022\)](#). The cool planet climate regime is characterised by a globally homogeneous formation of cloud condensation nuclei that leads to a globally homogeneous cloud coverage. WASP-96b has some day-to-night

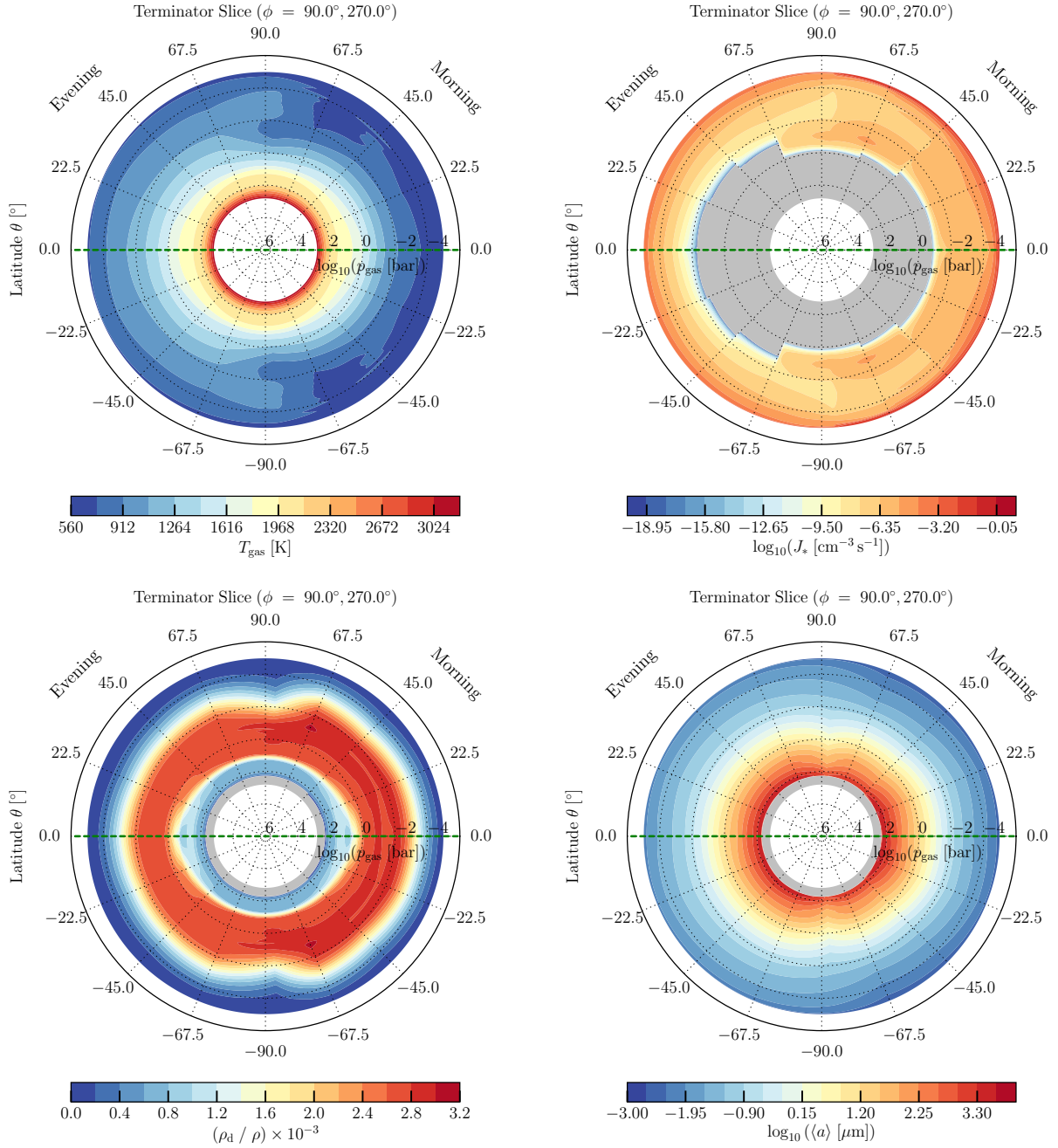


Fig. 2. WASP-96b cloud maps in 2D terminator slices as a result of the microphysical cloud model. *Top left:* local atmospheric gas temperature and gas pressure (T_{gas} , p_{gas}). *Top right:* total mineral seed formation (nucleation) rate, $J_* = \sum_i J_i$ ($\text{cm}^{-3} \text{s}^{-1}$) ($i = \text{TiO}_2, \text{SiO}, \text{NaCl}, \text{KCl}$). *Bottom left:* cloud particle-to-gas mass ratio ρ_d/ρ . *Bottom right:* mean cloud particle radius $\langle a \rangle$ (μm).

temperature difference, as shown in Fig. 1. The day-to-night temperature difference causes a temperature difference in the evening and morning terminator regions, as shown in the 2D terminator slice plot for the local gas temperature in Fig. 2 (top left). The evening terminator is affected by the warm gas being advected from the dayside to the nightside, and the morning terminator by the cold gas coming from the nightside. This causes a slightly ellipse-shaped high-temperature area in the equatorial regions ($\theta = 0^\circ$).

3.2. Mineral clouds on WASP-96b

In this section, we discuss the results for mineral cloud formation in the hot Saturn WASP-96b. This enables a detailed insight into

the cloud properties that are likely to shape the JWST spectrum of the planet.

3.2.1. Very mildly asymmetric cloud coverage and mildly non-homogeneous cloud properties

Firstly, we observe that cloud condensation nuclei (CCNs) form for all the 1D profiles used here to probe the cloud formation in the 3D atmosphere of WASP-96b (Fig. 2, top right). This is in stark contrast to ultra-hot Jupiters such as WASP-18b and HAT-P-7b, but in line with other hot Jupiters such as HD 189733b and HD 209458 b. Secondly, the rate of seed formation differs between the day- and the nightside because of

the different thermodynamic conditions. The morning terminator regions have a somewhat larger atmospheric volume where efficient formation of CCNs takes place compared to the evening terminator (i.e. at the morning terminator, the region of efficient nucleation extends to deeper pressures than at the evening terminator). The nucleation rate, J_s , follows the asymmetric morning and evening terminator temperature differences.

After the CCNs are formed, they grow to macroscopic cloud particles through condensation. These cloud particles fall into the atmosphere towards higher pressures where growth may accelerate before the cloud particles evaporate, where their materials become thermally unstable at the cloud base (at $p_{\text{gas}} \approx 10^{2.2}$ bar, consistently around the terminator). Therefore, the extension of the cloud is determined by the atmospheric volume that is populated by cloud particles (Fig. 2, bottom left), not by where the CCNs form (Fig. 2, top right). Mean cloud particle sizes range from $0.3 \mu\text{m}$ at $p_{\text{gas}} = 10^{-2}$ bar, to $15 \mu\text{m}$ at 1 bar and 0.1 mm at the cloud base at $p_{\text{gas}} = 158$ bar.

The cloud extension is affected by the vertical mixing efficiency, but also by material properties such as the cloud particle porosity. The vertical mixing counteracts the element depletion of the gas phase by cloud formation, which would inhibit the continuous presence of clouds in an atmosphere (see Sect. 3.3 in [Woitke & Helling 2003](#)). [Samra et al. \(2020\)](#) demonstrated that a highly porous (low density) cloud would expand the cloud layer upwards because of the increased surface area provided by porous cloud particles. However, the cloud base is unaffected as it is determined by thermal stability. High-porosity cloud particles would also have a larger mean particles size and would result in a somewhat higher cloud particle-to-gas mass ratio.

Figure 2 (lower left) shows that the cloud particle mass load (in terms of the cloud particle-to-gas mass ratio ρ_d/ρ) of the WASP-96b model atmosphere appears rather symmetrically distributed as a result of the homogeneous thermodynamic structure that is suggested by the 3D GCM for WASP-96b. However, there is still a slight asymmetry between the two terminators in the peak cloud particle mass load that is due to the increased particle surface area from the higher nucleation rate on the morning terminator.

3.2.2. General material composition of cloud particles

The 2D terminator slice plots in Fig. 3 visualise the cloud particle material compositions in units of material volume fraction, V_s/V_{tot} (Eqs. (25) and (26) in [Helling & Woitke 2006](#) and Eq. (6) in [Helling et al. 2008](#)). We did not consider carbon condensate species and have demonstrated the mineral CCN formation is more prominent in oxygen-rich atmospheres than the formation of hydrocarbon hazes ([Helling et al. 2020](#)). The 16 materials that are considered to contribute to the bulk growth of the cloud particles for our WASP-96b model are collected into four groups: metal oxides, silicates, high temperature condensates and salts (for details, see the caption of Fig. 3). With a view to the possible observability of cloud particles through their spectral fingerprints, important results are listed below:

- Cloud particles are made of a mix of all materials that are thermally stable at the local ($T_{\text{gas}}, p_{\text{gas}}$).
- The silicate materials ($\text{MgSiO}_3[\text{s}]$, $\text{Mg}_2\text{SiO}_4[\text{s}]$, $\text{Fe}_2\text{SiO}_4[\text{s}]$, and $\text{CaSiO}_3[\text{s}]$) dominate the material composition of the cloud particles that form the clouds of WASP-96b almost everywhere. Their dominant contribution, however, varies between 40% in the low-pressure regions ($p_{\text{gas}} \lesssim 10^{-1.5}$ bar

on the morning terminator, and $p_{\text{gas}} \lesssim 10^{-2.5}$ bar on the evening terminator) and $>90\%$.

- The metal oxides ($\text{SiO}[\text{s}]$, $\text{SiO}_2[\text{s}]$, $\text{MgO}[\text{s}]$, $\text{FeO}[\text{s}]$, and $\text{Fe}_2\text{O}_3[\text{s}]$) are the second most important materials reaching a contribution of no more than 40% in the same locations in which the silicates reach their 40% level.
- The high-temperature condensates ($\text{TiO}_2[\text{s}]$, $\text{Fe}[\text{s}]$, $\text{FeS}[\text{s}]$, $\text{Al}_2\text{O}_3[\text{s}]$, and $\text{CaTiO}_3[\text{s}]$) dominate the material composition of the cloud particles at the cloud base where all silicates, metal oxides, and salts have evaporated.
- Salts ($\text{KCl}[\text{s}]$ and $\text{NaCl}[\text{s}]$) are negligible as bulk species.

We therefore suggest that the cloud particles in the low-pressure regions that are accessible by transmission spectroscopy are dominated by a mix of $\approx 40\%$ metal oxides and 40% silicates. These particles have a mean particle size of $\lesssim 10^{-2} \mu\text{m}$ throughout the terminator region that is accessible by transmission spectroscopy.

3.3. Mineral ratios and the mean molecular weight

Mineral ratios (element ratios) such as Si/O, Mg/O, and Fe/O and the carbon-to-oxygen ratio, C/O, may help to link observations to evolutionary stages of exoplanets ([Khorshid et al. 2021](#); [Öberg & Bergin 2016](#)). The challenge with this inference is that observations have only provided snippets of the atmosphere spectrum so far, that is, information about limited wavelength intervals. Consequently, inferences of element ratios often hinge on retrieved abundances of individual gas species. This situation may change with the recent JWST observations, although the new JWST observations are still limited in range as they are only from NIRISS/SOSS.

The carbon abundance can only exceed the oxygen abundance if either carbon is produced (like in AGB stars), is inserted in another way into the system (e.g. meteoritic influx), or if the oxygen is simply reduced below the original carbon-abundance level. The latter might occur if the planet already starts out with a primordial atmosphere that is depleted in oxygen due to the formation of $\text{H}_2\text{O}/\text{CO}$ ices inside the planet-forming disk. The accretion of the gaseous envelope from this oxygen-depleted gas and further processing of the atmospheric gas into clouds can then lead to a $\text{C/O} > 1$ ([Helling et al. 2014](#)).

Compared to the Si/O, Mg/O, and Fe/O ratios, C/O is not affected as strongly. The lower abundances of Si, Mg, and Fe are more significantly depleted by condensation than oxygen (Fig. 4). However, the C/O ratio is higher in regions of cloud formation because the oxygen element is depleted from the gas phase through condensation (Fig. 4, bottom). The maximum value suggested by our simulations is $\text{C/O} = 0.75$, which also occurs in the upper part of the modelled atmosphere and thus likely in the optically thin atmosphere observed in transmission. We note that the set of Y and T-type brown dwarfs [Guillot et al. \(2022\)](#) also appears to reach supersolar C/O.

A decrease below the undepleted (solar) C/O value of 0.55 would suggest an increased amount of oxygen in the atmosphere or a substantial decrease of the carbon in the atmosphere. [Molaverdikhani et al. \(2020\)](#) showed for the ultra-hot Jupiter HAT-P-7b that advection-driven non-equilibrium may occur for H_2O , but C/O would be determined by the oxygen depletion by cloud formation.

We note that in this section, the local gas-phase C/O is discussed, which includes the depletion of oxygen by cloud formation. The retrieval procedure in Sect. 4.1 addresses the bulk C/O, which is indicative of the formation history of the planet. We demonstrate in Sect. 4.2, however, that the retrieval

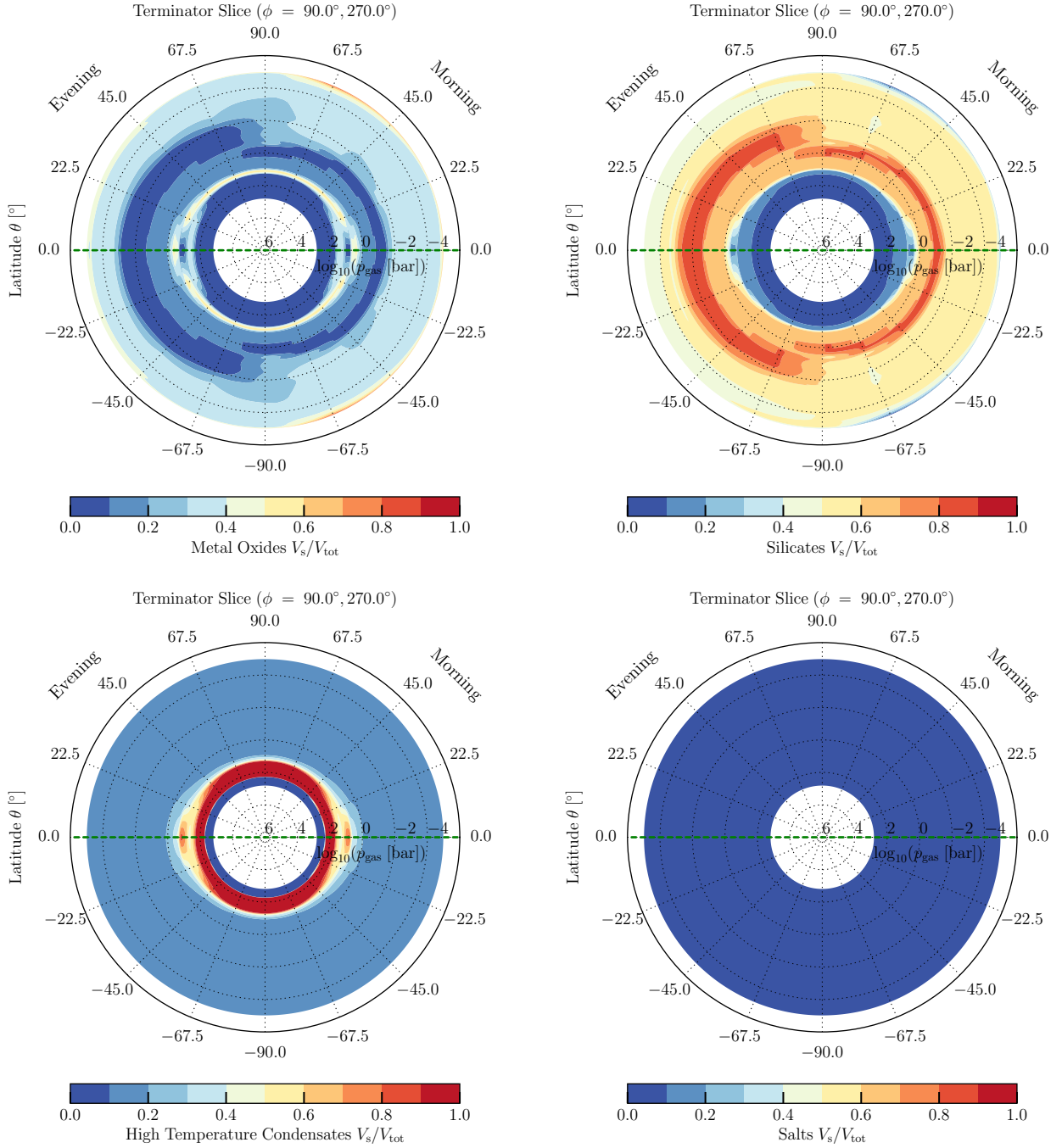


Fig. 3. Volume ratio of the cloud-forming materials for WASP-96b in 2D terminator slices for the same models as in Fig. 2, materials are grouped as in Helling et al. (2021). *Top left:* metal oxides ($s = \text{SiO}[\text{s}], \text{SiO}_2[\text{s}], \text{MgO}[\text{s}], \text{FeO}[\text{s}], \text{Fe}_2\text{O}_3[\text{s}]$). *Top right:* Silicates ($s = \text{MgSiO}_3[\text{s}], \text{Mg}_2\text{SiO}_4[\text{s}], \text{Fe}_2\text{SiO}_4[\text{s}], \text{CaSiO}_3[\text{s}]$). *Bottom left:* high-temperature condensates ($s = \text{TiO}_2[\text{s}], \text{Fe}[\text{s}], \text{FeS}[\text{s}], \text{Al}_2\text{O}_3[\text{s}], \text{CaTiO}_3[\text{s}]$). *Bottom right:* salts ($s = \text{KCl}[\text{s}], \text{NaCl}[\text{s}]$.)

suggests two solutions as best fits (or most probable fits) to the observed data. The mean molecular weight remains that of an H_2 -dominated gas until deep in the atmosphere because the upper atmosphere temperatures remain >2000 K (see Fig. 1).

3.4. Where clouds on WASP-96b become optically thick

We computed the pressure at which the optical depth of the clouds reaches unity ($p_{\text{gas}}(\tau(\lambda) = 1)$) based on our microphysical cloud model. This is hereafter referred to as the ‘cloud deck’.

This definition is aligned with the cloud top pressure recovered in retrievals, although the exact physical interpretation of these parameters depends on the cloud model and observation geometry (Barstow & Heng 2020). We used the vertically integrated optical depth for individual 1D profiles; this neglects 3D effects. However, given the homogeneity of cloud formation in these models of WASP-96b, the effects of a slanted observing geometry can be corrected for through a correction factor (Fortney 2005). Furthermore, the optical depths derived here depend on the computational domain of the GCM because above this level, we are unable to model cloud formation. Previously,

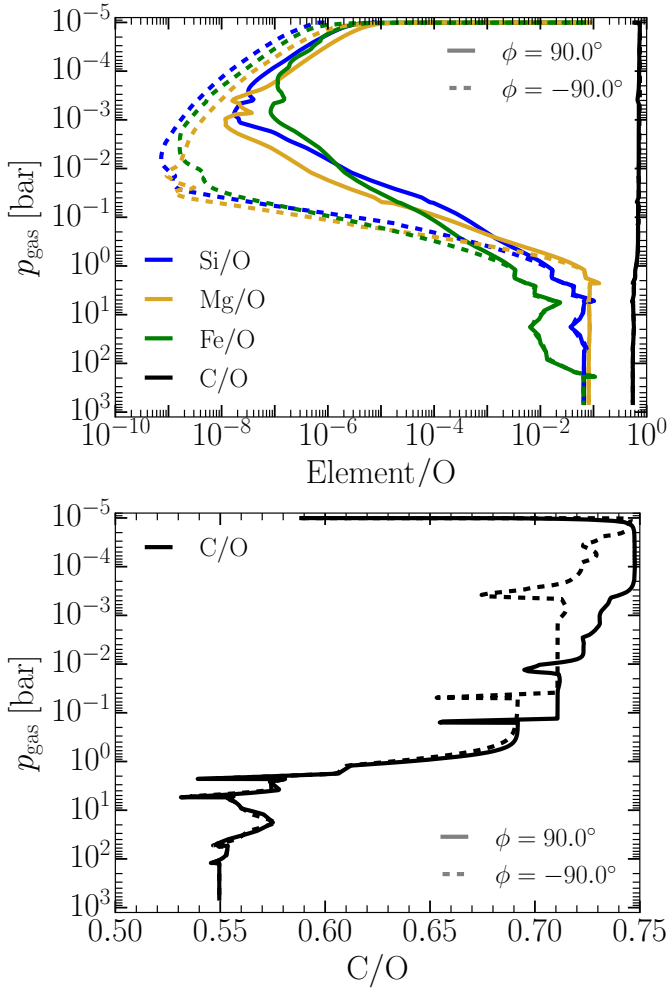


Fig. 4. Gas phase abundance ratios for morning ($\phi = -90.0$, dashed lines) and evening ($\phi = 90.0$, solid lines) terminators. Some morning-to-evening terminator differences exist. *Top:* mineral ratios Si/O, Mg/O, and Fe/O are strongly affected by element depletion due to cloud formation. *Bottom:* C/O ratio appears to be less affected, but oxygen is two orders of magnitude more abundant in a solar set of element abundances. C/O is therefore shown on a linear scale, where C/O=0.55 is the solar value.

Helling et al. (2022) have shown that the restricted GCM domains miss the mineral haze layer at higher altitudes.

The four key points around the equator ($\theta = 0.0^\circ$) of WASP-96b (Fig. 5 top left) show that for wavelengths $<4 \mu\text{m}$, the cloud deck is indeed consistent. Nonetheless, in this range, the cloud deck still shows a substantial slope with wavelength. For example between $0.3\text{--}5 \mu\text{m}$ for the morning terminator, the cloud deck pressure varies between $1.3 \times 10^{-4}\text{--}6 \times 10^{-3}$ bar. This suggests that flat cloud decks are a poor fit in this wavelength range, which becomes more important in an era where broader wavelength coverage is possible with a single mission. In the mid-IR, this is different: spectral differences may be expected within the silicate feature wavelength range, which will be visible with NIRSpec, NIRCam⁶, ARIEL⁷, and MIRI. *Spitzer* sits right on this silicate edge at $\sim 4 \mu\text{m}$, which may complicate a combination of datasets. In particular, the cloud deck from $4\text{--}8 \mu\text{m}$ shows differences of nearly an order of magnitude in pressure at the two terminator limbs.

⁶ Near Infrared Camera.

⁷ Atmospheric Remote-sensing Infrared Exoplanet Large-survey.

The high-pressure cloud decks (or cloud-free atmospheres) previously retrieved by Nikolov et al. (2018) in order to fit the Na line (dashed vertical blue line) are inconsistent with microphysical cloud formation. At the Na line, the model produces a cloud deck at $\sim 2.5 \times 10^{-4}$ bar, whereas pressures as high as 10^{-2} bar are needed to fit the observed pressure broadening. However, given the pressure–temperature structures shown in Fig. 1, simple thermal stability arguments will expect clouds to form. Retrievals cannot simply infer condensable-favouring global temperatures and claim deep cloud decks or cloud-free atmospheres without proposing some mechanism for cloud suppression.

We therefore explored three parameters: vertical mixing efficiency, cloud particle porosity, and metallicity, and their effect on the cloud deck pressure level. The vertical mixing efficiencies were reduced by increasing the mixing timescale. This was done by introducing a mixing scale factor f_{mix} , such that the new mixing timescale is

$$\tau_{\text{mix}}^{\text{eff}} = \frac{1}{f_{\text{mix}}} \tau_{\text{mix}}, \quad (1)$$

where τ_{mix} is the mixing timescale from the GCM derived the same way as in Helling et al. (2022). Alternatively, using $K_{zz} = H_p \tau_{\text{mix}}$ implies that similarly K_{zz} is reduced by factors of f_{mix} . Reduction of the vertical mixing efficiencies ($f_{\text{mix}} = 0.1, 0.01$) reduced the cloud deck height by an order of magnitude in pressure, but otherwise maintained the wavelength dependence. The mechanism for this inefficient mixing requires further investigations.

We included the porosity of cloud particles as described in Samra et al. (2020). This reduced the effective material density of cloud particles ρ_s^{eff} through the porosity factor f_{por} , $\rho_s^{\text{eff}} = \rho_s(1 - f_{\text{por}})$.

Mass conservation ensures that the radii of the cloud particles were also increased correspondingly. In addition, the porosity of the cloud particle was incorporated into the opacity calculation by including the vacuum refractive index into effective medium theory (Bruggeman 1935; Looyenga 1965) in proportion to the porosity factor of the particle.

Highly porous particles reduce the opacity of the clouds, even with a higher cloud mass load and a higher onset of bulk growth, as was the case in Samra et al. (2020), although the effect here is substantially larger than in the hotter atmosphere ($T_{\text{eff}} = 1800 \text{ K}$) presented there. Unlike reductions in mixing efficiency, the increased cloud particle porosity affects the wavelengths $>4 \mu\text{m}$ non-uniformly, the cloud deck pressure level at the silicate feature wavelengths is particularly affected by compact versus porous cloud particles.

The porosity and shape of cloud particles (or more generally aerosols) in exoplanet atmospheres remain uncertain (Gao et al. 2021). However, there is some tentative evidence of porous cloud particles (generated through collisions) as an explanation for the flat spectrum of the mini-Neptune GJ-1214b (Ohno et al. 2020). As shown in Samra et al. (2022), however, collisions in exoplanet atmospheres when turbulence is included are expected to be destructive and not to produce larger aggregate particles. However, hazes of fractal aggregates have been inferred for a number of bodies in the Solar System and for exoplanets (e.g. Adams et al. 2019). Porosity has also been examined in other astrophysical contexts, such as protoplanetary disc dust (Woitke et al. 2016), but only a factor of 25% vacuum was assumed. Whether cloud particles may reach high (90%) porosities like this is unknown in general, but it still remains an effect that is important to consider when exoplanet observations are interpreted.

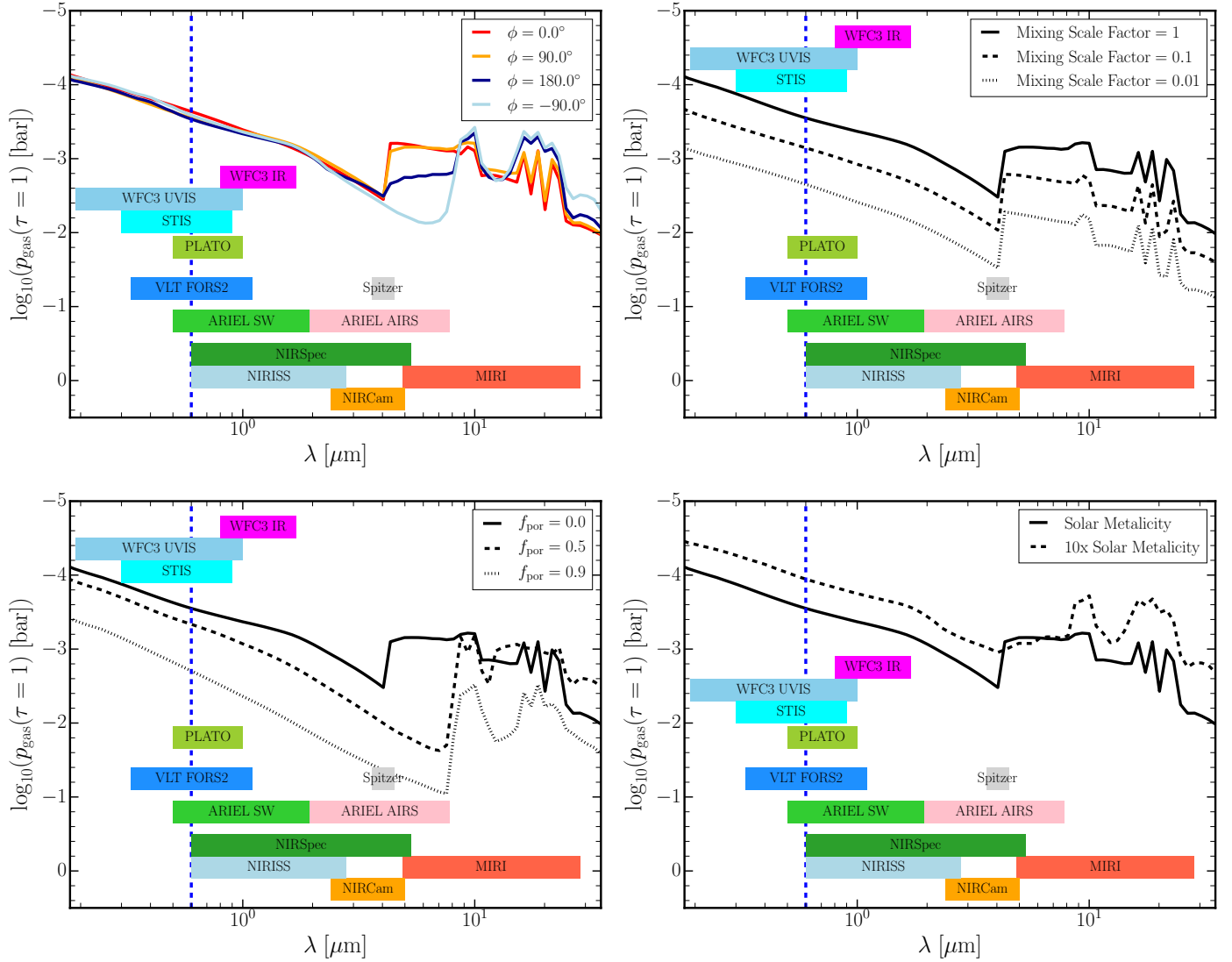


Fig. 5. Changing slope of the optically thick pressure levels ($p_{\text{gas}}(\tau(\lambda) = 1)$) within optical to mid-IR wavelengths (0.2–30 μm). The dashed blue line indicates the location of the sodium line, and the coloured bars show the wavelength ranges of various missions. *Top left:* $\tau(\lambda) = 1$ slopes for the morning and evening terminator, the substellar point ($\phi = 0^\circ$, red), and the antistellar point ($\phi = 180^\circ$, dark blue). The remaining plots show parameter studies for the evening terminator ($\phi = 90^\circ$, $\theta = 0^\circ$). *Top right:* different mixing efficiencies. *Bottom left:* effect of cloud particle porosity. *Bottom right:* effect of element abundances.

We assumed solar elemental abundances (Asplund et al. 2009) for the gas composition of the atmosphere so far. Nikolov et al. (2022) derived elemental abundances for the host star WASP-96 using FEROS⁸ spectra. These abundances are higher than the solar abundances of (Asplund et al. 2009) by a factor of $\sim 3\times$ solar at most (e.g. Mg and Mn; see their Table 4). However, it is unclear whether stellar metallicities correlate with planetary atmosphere abundances (Teske et al. 2019). Nonetheless, we examined the effect of a higher metallicity for cloud formation in the atmosphere using a ten times solar metallicity for the planetary atmosphere. This was done by increasing the abundance of everything except H and He and renormalising to the H abundance. The metallicity for WASP-96b, based on formation arguments for lower-mass gas giant planets (e.g. Carone et al. 2021; Chachan et al. 2019; Schneider & Bitsch 2021), is expected to be superstellar. The higher metallicity increases the cloud formation and leads to a higher cloud deck (bottom right panel

of Fig. 5), making it even harder to reconcile with supersolar retrievals.

4. Clouds affecting the 0.3–5 μm spectra

Solving the radiative transfer problem through a prescribed atmospheric structure with clouds allows us to explore the effect of cloud properties on the possible spectral appearance of WASP-96b within the wavelength range that has been explored with VLT/FORS2, HST/WFC3, and *Spitzer* so far. This procedure is known as forward-modelling within the retrieval community. The ARCiS (Min et al. 2020; Ormel & Min 2019) framework was applied here. We further investigated the possibility of finding a solution to the VLT/FORS2, HST/WFC3, and *Spitzer* data including the effect of clouds using a retrieval setup that included a parametrised cloud formation routine.

Retrieval studies of the HST/WFC3 and *Spitzer*/IRAC transmission spectra of WASP-43b also previously struggled to find evidence for the presence of clouds in the atmospheric

⁸ Fiber-fed Extended Range Optical Spectrograph.

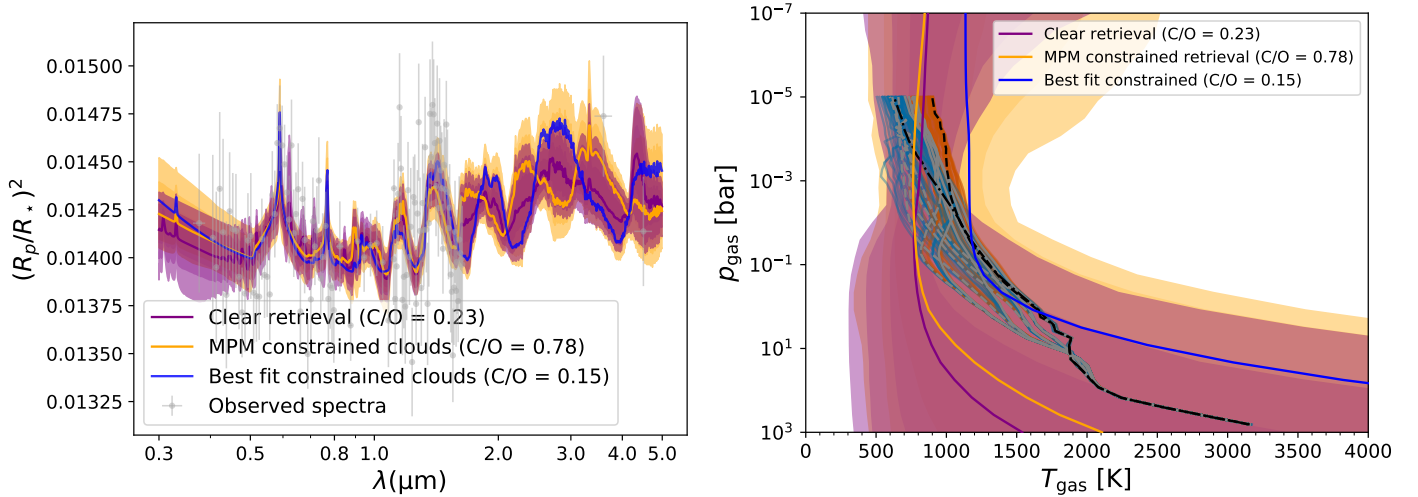


Fig. 6. Best-fit models (1, 2, and 3 σ bounds shading) retrieved with ARCiS from the Nikolov et al. (2022) pre-JWST observations. ARCiS retrieval without clouds (purple) and with cloud formation (orange; as described in Ormel & Min 2019). Both retrievals assume equilibrium chemistry. The retrieved parameters for the cloud formation are shown in Fig. B.1, and for the case without clouds, they are shown in Fig. B.2. MPM refers to the median probability model, which is slightly different from the best-fit model; see text. *Left:* retrieved spectrum. *Right:* retrieved pressure–temperature profile. The GCM temperature–pressure structures are over-plotted for reference in the same colour scheme as in Fig. 1.

spectra (Kreidberg et al. 2014; Chubb et al. 2020a), at least at the pressure levels probed by these observations. However, works like Helling et al. (2020) studied the formation of mineral clouds and hydrocarbon hazes in the atmosphere of WASP-43b and demonstrated that it is rather unlikely that WASP-43b is free of clouds. Robbins-Blanch et al. (2022) performed a detailed study of the effects of clouds on emission phase curve spectra of WASP43b by computing various forward models for clear and cloudy atmospheres using PICASO (Batalha et al. 2020; Batalha & Rooney 2020). They found that cloudy phase curves, produced from 3D models, provide much better agreement with the WFC3 and *Spitzer* nightside data than cloud-free models.

4.1. Retrieval results

We present the results of our retrievals of the observed VLT (Nikolov et al. 2018), HST, and *Spitzer* (Nikolov et al. 2022) transit spectra using the atmospheric retrieval and modelling code ARCiS (Min et al. 2020; Ormel & Min 2019). Molecular and atomic opacities in the form of k-tables were used from various sources such as ExoMol (Tennyson et al. 2020, 2016), HITEMP (Rothman et al. 2010), HITRAN (Gordon et al. 2021), MoLLIST (Bernath 2020), and NIST Kramida et al. (2013), as detailed in Chubb et al. (2021). We included the following set of species (and opacities computed by the listed line list) in both sets of retrievals, which computed spectra under the assumption of equilibrium chemistry using GGChem (Woitke et al. 2018): H_2O (Polyansky et al. 2018), CO_2 (Yurchenko et al. 2020), CH_4 (Yurchenko et al. 2017), CO (Li et al. 2015), OH (Bernath 2020; Yousefi et al. 2018), AlO (Patrascu et al. 2015), K (Allard et al. 2016, 2019; Kramida et al. 2013), Na (Allard et al. 2019; Kramida et al. 2013), NH_3 (Coles et al. 2019), TiO (McKemmish et al. 2019), VO (McKemmish et al. 2016), H_2S (Azzam et al. 2016), HCN (Barber et al. 2014), PH_3 (Sousa-Silva et al. 2015), C_2H_2 (Chubb et al. 2020b), CN (Brooke et al. 2014), and SiO (Barton et al. 2013; Yurchenko et al. 2021).

We ran two different retrievals: a constrained cloud formation retrieval following the method of Min et al. (2020) on the combined HST, VLT, and *Spitzer* data set (including the HST-VLT offset) of Nikolov et al. (2022), and a completely clear

(no parameters describing clouds were included) retrieval for comparison. Both retrievals assumed chemical equilibrium for the gas-phase chemistry, which was computed after the cloud formation computations. The parameters we retrieved and their priors can be found in Table 1. The best-fit retrieved spectra, with 1, 2, and 3 σ shading, are shown in Fig. 6 (left). The observed spectra are plotted for comparison. Our retrieved posterior distributions can be found in Fig. B.1 for the cloud formation and in Fig. B.2 for the clear atmosphere. The first four parameters in Figs. B.1 and B.2 describe the pressure–temperature parametrisation of Guillot (2010). These were used to construct the pressure–temperature profiles for the two retrievals given in Fig. 6 (right). The pressure–temperature profiles from the GCM used in our atmospheric modelling and cloud formation models are plotted for comparison. They can also be compared to Fig. 5 of Nikolov et al. (2022). The clear retrieval pressure–temperature profile in our Fig. 6 (right) appears to be very similar to their retrieved pressure–temperature profile, which also assumes equilibrium chemistry.

The two panels of Fig. 6 illustrate solutions from the cloud formation retrieval based on slightly different model outputs. The best-fit model has the lowest χ^2 when compared to the observations. However, other possible solutions can also fit the data similarly well. The median probability model (MPM; Barbieri & Berger 2004; Barbieri et al. 2021) is based on the posterior distributions shown in Fig. B.1 and represents an alternative region of parameter space for the cloud formation retrieval presented in this work. In particular, the posterior distribution for the retrieved C/O has two potential solutions; one with high C/O (~ 0.78 ; the MPM solution), and one with lower C/O (~ 0.15 ; the best-fit solution). The left panel of Fig. 6 shows that the retrieved best-fit and MPM spectra are very similar in the region covered by the VLT and HST observations, and they fit the observed data similarly well. However, they deviate in the region of the spectra for wavelengths longer than the HST data. The same is true for the clear retrieval; it deviates most in the region that is not covered by the observed data. It is therefore difficult to distinguish them based on the observed data. The bottom two panels of Fig. C.1 give the molecular abundances (volume-mixing ratios) as a function of pressure for the MPM (left) and best-fit (right) solutions. The

variations in the CO and CH₄ abundances between these two solutions are particularly large. The primary spectral features of both these molecules are not in the region of the spectra covered by the HST and VLT observations; around 2.3 and 5 μm for CO, and around 3.3 μm for CH₄. As illustrated by Gasman et al. (2022), other absorption features of CH₄ that are present in the region of the HST data are often masked by stronger H₂O features. Figure C.2 shows the volume-mixing ratios of various molecules predicted to be present at the equator of the morning (left) and evening (right) terminators, based on the GCM and kinetic cloud models of this work. CO is expected to be abundant in both cases, along with H₂O at most altitudes. These are more similar to the lower C/O retrieval solution in the bottom left panel of Fig. C.1. Figure C.1 also shows that the difference in H₂O abundance between the two retrieval solutions can have a noticeable effect on the spectra, again in particular in the region longward of 1.7 μm. This highlights the benefits of the JWST observations of WASP-96b (Pontoppidan et al. 2022), which do cover this region.

The right-hand panel of Fig. 6 shows that the cloud formation retrieval solution with the lower C/O has a higher atmospheric temperature than the solution with the higher C/O. This is due to the constraints placed by the cloud formation scheme. The same does not apply to the clear atmosphere retrieval; there is no constraint on the temperature based on what types of clouds are expected to form, and a lower temperature is therefore preferred. The cloud formation model with the lower C/O necessitates a higher atmospheric temperature at the pressure layers that are probed by the observations. This is because a low C/O and therefore an abundance of oxygen would mean that K- and Na-silicate clouds are expected to form if the temperature is low enough. However, the strong gas-phase Na and K spectral features suggest that these species of clouds either have not formed efficiently in this atmosphere, at least not at a very large abundance to take all the Na and K away from the gas phase, or they form, but are optically thin enough such that the gas-phase Na and K is still observable. A recent observation of planetary mass companion VHS 1256-1257 b using the JWST NIRSpec IFU and MIRI MRS modes revealed solid-state silicate features in the longer wavelength part of the atmospheric spectrum (Miles et al. 2022). This was considered as strong evidence for small silicate particles in the brown dwarf atmosphere; as demonstrated by works such as Min et al. (2004), small particles lead to lower overall extinction across the spectra, but a more prominent silicate feature. The atmospheric mixing is described by a $K_{zz} = 10^8 \dots 10^9 \text{ cm}^2 \text{ s}^{-1}$. These observations suggest that silicate clouds do form in substellar hot atmospheres and that it is possible to directly observe their spectral signatures with the JWST.

This is either due to a lower C/O and therefore due to less oxygen that is available for these clouds to form from, or a lower C/O but a high enough atmospheric temperature to stop them from forming in abundance. We also ran a retrieval with cloud formation, but without the cloud species that condense Na and K. In this case, the lower C/O solution was preferred because no constraints were placed based on the temperature of formation for these types of clouds. It should be noted that the C/O for the cloud formation retrievals is the bulk C/O, that is, before clouds are allowed to form. Clouds will generally deplete oxygen from the atmosphere, so that the retrieved C/O without cloud formation constraints (but where clouds should be present based on atmospheric temperature, such as for the clear retrieval) will be expected to be retrieved higher than the bulk C/O. The models with the lowest C/O ratio show significant H₂O features in the

region that is not covered by the HST and VLT data, which is not the case for the high C/O case. Since the newly observed JWST ERO data appear to show strong H₂O spectral signatures (Pontoppidan et al. 2022), a situation with a lower C/O and higher atmospheric temperature could be preferred. A more detailed study of this JWST spectrum of WASP-96b in the near future should be very informative.

The reduced- χ^2 value was very similar for the clear and the cloud formation retrievals (1.08 and 1.09, respectively), indicating that both can fit the observed data equally well. The cloud formation retrieval is not considered statistically significant in comparison to the clear retrieval, however, that is, including additional parameters to characterise the clouds is not justified by a significant increase in how well the model fits the data. This has previously led to the conclusion that the atmosphere must be clear. Based on expectations from detailed simulations of cloud formation in the atmosphere of WASP-96b, as demonstrated in this paper, it would be very surprising from a physical point of view if the atmosphere were completely clear. We therefore try to offer some explanations to confront this apparent contradiction between what models predict (a cloudy atmosphere) and what the observed data appear to show (a clear atmosphere).

Firstly, in Fig. B.1, the cloud diffusivity K_{zz} (which represents the vertical mixing strength of cloud particles) is constrained to be no higher than around $2 \times 10^6 \text{ cm}^2 \text{ s}^{-1}$. This corresponds to the reduced mixing scenario explored in Fig. 5 (top right). A reduction in vertical mixing of cloud particles settles the cloud layer farther down in the atmosphere, thus reducing its optical effects on blocking or muting gas-phase molecular or atomic signatures. We further illustrate this by computing a forward model using our best-fit cloud formation retrieval, with varying values of K_{zz} (Fig. 7). Figure 8 shows the pressure level at which the optical depth of the atmosphere reaches unity (i.e. it becomes optically thick) as a function of pressure for the models. Figure 7 shows that lower values of K_{zz} , around $2 \times 10^6 \text{ cm}^2 \text{ s}^{-1}$, allow for a clear detection of the Na doublet at around 0.6 μm, with the atomic line broadening by H₂ and He clearly visible. Increasing K_{zz} mutes this and other gas-phase spectral features. Our retrieved value of vertical cloud diffusion parameter K_{zz} is between 1.7×10^5 and $1.8 \times 10^6 \text{ cm}^2 \text{ s}^{-1}$, within 1 σ bounds, and between 2.1×10^4 and $2.5 \times 10^7 \text{ cm}^2 \text{ s}^{-1}$ within 3 σ bounds. The priors on K_{zz} were $10^5 \dots 10^{12} \text{ cm}^2 \text{ s}^{-1}$, which means that these values are at the lower edge of the priors. In comparison, the K_{zz} values used in our microphysical model range between $10^7 \dots 10^9 \text{ cm}^2 \text{ s}^{-1}$. These values are comparable to the directly imaged brown dwarf result from Miles et al. (2022). With a reduction by a factor of 10^{-2} , we therefore find some agreement between the retrieved K_{zz} and a microphysical model, but the deeper cloud deck (as shown in Sect. 3.4) is still higher than shown in Fig. 8. We reiterate that the mechanism for this reduced mixing is uncertain.

Figure B.1 shows that the free parameter, the integrated cloud particle nucleation rate $\dot{\Sigma} [\text{g cm}^{-2} \text{ s}^{-1}]$, is not particularly well constrained by the retrieval, but a lower value is preferred. The nucleation rate, $J_i (\text{cm}^{-3} \text{ s}^{-1})$ for $i = \text{TiO}_2, \text{SiO}, \text{KCl}, \text{and NaCl}$, in our kinetic cloud formation model is not a parameter, but we calculated the local nucleation rate instead (see Sect. 2) according to the local thermodynamic properties ($T_{\text{gas}}, p_{\text{gas}}$). The integrated cloud particle nucleation rate can be calculated as

$$\dot{\Sigma} = \int \sum_i m_i J_i dz. \quad (2)$$

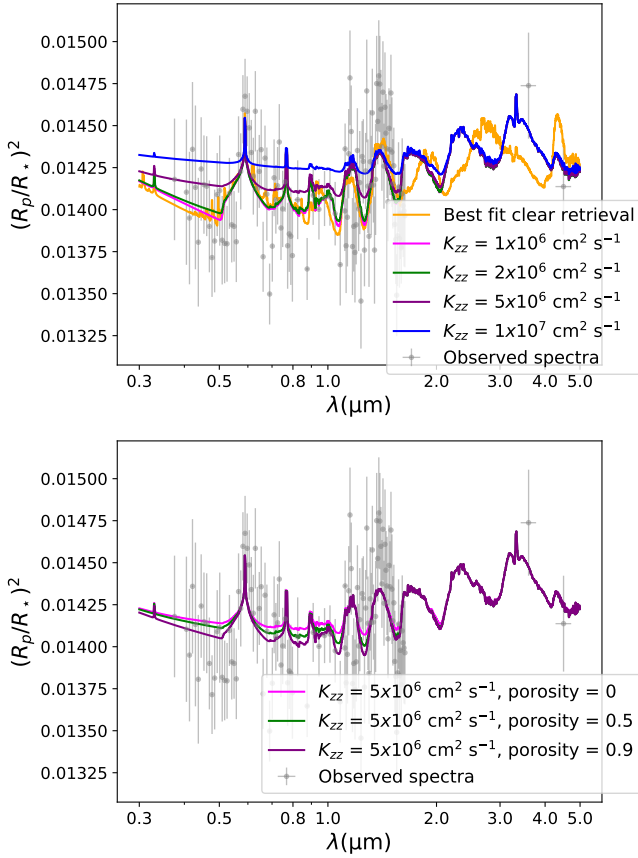


Fig. 7. Best-fit synthetic spectrum from the constrained retrieval of the Nikolov et al. (2022) data (VLT, HST, and *Spitzer*) with varying values of cloud diffusivity, K_{zz} , (top), and for a varying cloud particle porosity for atmospheric models with a cloud diffusivity $K_{zz} = 5 \times 10^6 \text{ cm}^2 \text{ s}^{-1}$ (bottom).

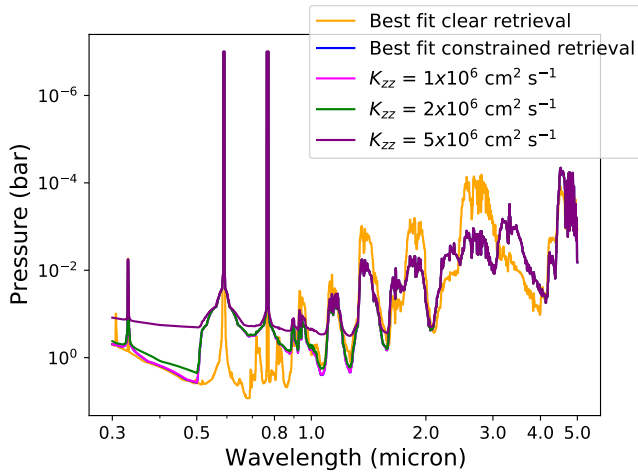


Fig. 8. Same cloud formation setups with varying cloud diffusivity K_{zz} as for Fig. 7, but this time showing the pressure levels at which optical depth τ reaches unity, as a function of wavelength. The sharp drop in the Na lines (green line) is artificial and caused by the cutoff in the available opacity data.

Here, the summation is over the four nucleation species considered ($i = \text{TiO}_2, \text{SiO}, \text{NaCl}, \text{and KCl}$), with the mass of individual monomer species m_i and the respective nucleation rates J_i . The integration depends on the computational volume of the GCM. The cloud extension is therefore hidden within the $\dot{\Sigma}$ parameter. Using this, the terminator profiles (both morning

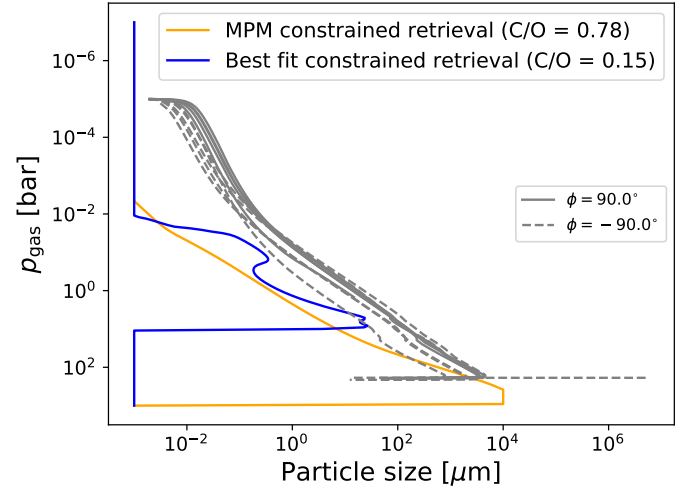


Fig. 9. Average particle sizes from the constrained retrieval with ARCiS for the MPM (yellow) and the best-fit (blue) models. Surface-averaged particle size $\langle a \rangle_A$ results from the kinetic cloud formation model (grey) and for the evening ($\phi = 90.0^\circ$, solid) and morning terminators ($\phi = -90.0^\circ$, dashed) are over-plotted.

and evening) from the GCM give integrated nucleation rates of between $1.49 \times 10^{-15} \dots 4.56 \times 10^{-14} \text{ g cm}^{-2} \text{ s}^{-1}$. This is in broad agreement with the retrieved values for the integrated nucleation rate, although the retrieval slightly favours lower values 5×10^{-17} to $6 \times 10^{-14} \text{ g cm}^{-2} \text{ s}^{-1}$, within 1σ bounds. Figure B.1 shows that the lower retrieved values of $\dot{\Sigma}$ are towards the bottom of the prior region (lower limit of $10^{-17} \text{ g cm}^{-2} \text{ s}^{-1}$). This is because the retrieval essentially tries to minimise the formation of clouds in an atmosphere that, as the kinetic cloud formation model shows, should form clouds.

Another factor that might influence the observed spectra is the porosity of the cloud particles. The cloud particles in our retrievals are all assumed to be non-porous (porosity = 0). Figure 7 shows, however, that increasing the porosity of cloud particles acts in a similar way to reducing the vertical mixing of cloud particles. The clouds become more transparent, which reduces their optical thickness as the porosity is increased. This particularly affects wavelengths shorter than around $2 \mu\text{m}$. This trend agrees with the lower cloud deck pressure found in Sect. 3.4 when the effects of cloud porosity were included. However, the effect here is greatly reduced when compared to Fig. 5 (lower left) because the cloud in the best-fit constrained model is already lower. The effect of cloud particle porosity has been explored further in works such as Samra et al. (2020). The plausibility of highly porous cloud particles has been discussed in Sect. 3.4.

Figure 9 shows the average particle size retrieved by ARCiS for the best-fit and MPM solutions as well as the surface-averaged particle size from the kinetic cloud formation model (Appendix A, Eq. (A.6) in Helling et al. 2020). The average cloud particle sizes from the kinetic cloud formation are larger than the retrieved average particle sizes at all pressures in the atmosphere. The kinetic cloud formation model experiences condensational growth for the cloud particles right from the top of the GCM domain 10^{-5} bar , and hence larger particle sizes. This contrasts with the results from ARCiS, where for both solutions, the growth of the average particle size does not start until deeper in the atmosphere. Both the kinetic cloud formation model and the ARCiS parametrised model use cloud condensation nuclei (CCN), the first step in cloud formation of size $\sim 10^{-3} \mu\text{m}$.

Figure 6 demonstrates that the retrieval result both (constrained and unconstrained) have large uncertainties in the retrieved pressure–temperature profiles. A temperature inversion might indicate clouds deeper in the atmosphere, which act to heat the upper layers and thus make them too hot for further cloud formation. This offers another explanation for why the atmosphere appears relatively cloud free from observations, but might still contain an abundance of clouds as predicted by our kinetic models.

4.2. Discussion

The compatibility of combining ground- and space-based data has been questioned in the case of WASP-96b by Yip et al. (2020a), who reported a significant offset between HST and VLT observations. The offset was also addressed by Nikolov et al. (2022), who performed a combined analysis of various observations (VLT, HST, and *Spitzer*), and also determined an offset between the HST and VLT observations. This data set (including their offset) was used in the retrievals of the present work.

Yip et al. (2020b) further demonstrated the potential issues with combining data from instruments such as HST/WFC3 and *Spitzer*/IRAC, which have no overlapping wavelength coverage. As the *Spitzer* data photometry points come with large uncertainties, use of them in retrievals to quantify abundances of species such as CO or CO₂ can lead to biases in retrievals, particularly when elemental abundances such as C/O are constrained. This has been highlighted previously by works such as Irwin et al. (2020). We therefore advise caution in the use of our retrieved value of C/O and await reduced spectra observed using the JWST for further analysis. Our results including cloud formation tentatively show two potential regions of parameter space that fit the observed pre-JWST data well: one with high C/O and a lower atmospheric temperature, and one with low C/O and a higher atmospheric temperature (in the region probed by the observations). The strong H₂O features in the region covered by the JWST observations could push towards the low C/O with a higher atmospheric temperature solution. We note that the best-fit analysis and retrieval of Nikolov et al. (2018) find a subsolar C/O in both cases. These retrieved C/O are bulk C/O (i.e. the C/O available before clouds are allowed to form), and therefore, a retrieved C/O without taking cloud formation into account will be higher than this bulk value. The bulk C/O is useful to be able to link to planet formation; a parametrised planet formation model such as that of Khorshid et al. (2021) can be coupled with retrieval codes such as ARCIS.

In Fig. C.1, we show the cloud species formed by the two solutions we found in our retrieval in the two upper panels. In the left column, we show the best-fit solution with C/O = 0.15 and a higher atmospheric temperature structure, and on the right, we show the MPM solution with C/O = 0.78 and a lower atmospheric temperature structure. The corresponding retrieved volume-mixing ratios of the gas-phase molecular species are given in the panels below. In the MPM case, the high C/O (planetary bulk C/O) indicates that not much oxygen is available to form clouds. Condensates such as Fe, SiO₂, Al₂O₃ (corundum), TiO₂, and VO are able to form, and the Na/K silicate and Mg/Ca silicate condensates do not have enough oxygen left to be able to form, even though the temperatures would allow them to do so. The best-fit case, on the other hand, has an abundance of oxygen in the atmosphere (low C/O). This allows the lower-temperature silicate clouds to form. The higher temperature profile does mitigate how much can form to some extent. Even with the Na/K silicate clouds that do form, the bottom left panel of Fig. C.1

shows that an abundance of gas-phase Na and K is still available to produce the strong atomic features seen in the observed spectra.

5. Conclusion

Based on our hierarchical modelling approach, which combines a 3D GCM atmosphere solution for WASP-96b with a kinetic, non-equilibrium formation model for mixed-material cloud particles, we suggest that WASP-96b is not cloud free, as previously instigated based on retrieval approaches. This suggestion is supported by applying the ARCIS retrieval framework to the same HST, *Spitzer*, and VLT data. The application shows that cloudy solutions do reproduce the observed spectra. More than one cloudy solution provides a good fit to the observational data, such that the retrieved solutions may not be unique, requiring more physical input. This is an important step towards discussing retrieval results from present and future JWST data.

Clouds in WASP-96b would cause the following effects within the JWST wavelength range:

- The cloud top varies with wavelength within the JWST NIRSpec and NIRISS spectral ranges for at least one order of magnitude in pressure;
- Clouds become optically thick at different pressures depending on wavelength. To achieve optically thin clouds down to $p = 10^{-2}$ bar, as implied by the sodium feature at $\sim 0.6 \mu\text{m}$, a moderate mixing efficiency is required;
- The long wavelength end of NIRSpec and short end of MIRI may probe atmospheric asymmetries between the limbs of the terminator on WASP-96b;
- WASP-96b could only be cloud free in the unlikely case of a truly static atmosphere, and only cloud free in the region probed by observations in the case of extremely low mixing efficiency or if a temperature inversion confines the clouds to higher pressures.

Acknowledgements. Ch.H., M.M., L.C., and A.D.S. acknowledge funding from the European Union H2020-MSCA-ITN-2019 under Grant Agreement no. 860470 (CHAMELEON). K.L.C. acknowledges funding from STFC, under project number ST/V000861/1. D.S. acknowledges financial support from the Austrian Academy of Science. The authors thank David Lewis for their helpful discussions on the manuscript.

References

- Adams, D., Gao, P., de Pater, I., & Morley, C. V. 2019, *ApJ*, 874, 61
 Allard, N. F., Spiegelman, F., & Kielkopf, J. F. 2016, *A&A*, 589, A21
 Allard, N. F., Spiegelman, F., Leininger, T., & Mollière, P. 2019, *A&A*, 628, A120
 Asplund, M., Grevesse, N., Sauval, A. J., & Scott, P. 2009, *ARA&A*, 47, 481
 Azzam, A. A. A., Yurchenko, S. N., Tennyson, J., & Naumenko, O. V. 2016, *MNRAS*, 460, 4063
 Baeyens, R., Decin, L., Carone, L., et al. 2021, *MNRAS*, 505, 5603
 Barber, R. J., Strange, J. K., Hill, C., et al. 2014, *MNRAS*, 437, 1828
 Barbieri, M. M., & Berger, J. O. 2004, *Ann. Stat.*, 32, 870
 Barbieri, M. M., Berger, J. O., George, E. I., & Ročková, V. 2021, *Bayesian Anal.*, 16, 1085
 Barstow, J. K., & Heng, K. 2020, *SSRev*, 216, 82
 Barton, E. J., Yurchenko, S. N., & Tennyson, J. 2013, *MNRAS*, 434, 1469
 Batalha, N., & Rooney, C. 2020, <https://doi.org/10.5281/zenodo.4206648>
 Batalha, N., Freedman, R., Lupu, R., & Marley, M. 2020, <https://doi.org/10.5281/zenodo.3759675>
 Bernath, P. F. 2020, *JQSRT*, 240, 106687
 Brandeker, A., Heng, K., Lendl, M., et al. 2022, *A&A*, 659, L4
 Brooke, J. S. A., Ram, R. S., Western, C. M., et al. 2014, *ApJS*, 210, 23
 Bruggeman, D. 1935, *Ann. Phys.*, 416, 636
 Carone, L., Baeyens, R., Mollière, P., et al. 2020, *MNRAS*, 496, 3582
 Carone, L., Mollière, P., Zhou, Y., et al. 2021, *A&A*, 646, A168

- Chachan, Y., Knutson, H. A., Gao, P., et al. 2019, *AJ*, 158, 244
- Chubb, K. L., & Min, M. 2022, *A&A*, 665, A2
- Chubb, K.L., Min, M., Kawashima, Y., Helling, Ch., & Waldmann, I. 2020a, *A&A*, 639, A3
- Chubb, K. L., Tennyson, J., & Yurchenko, S. N. 2020b, *MNRAS*, 493, 1531
- Chubb, K. L., Rocchetto, M., Al-Refaie, A. F., et al. 2021, *A&A*, 646, A21
- Coles, P. A., Yurchenko, S. N., & Tennyson, J. 2019, *MNRAS*, 490, 4638
- Fortney, J. J. 2005, *MNRAS*, 364, 649
- Fraine, J., Mayorga, L. C., Stevenson, K. B., et al. 2021, *AJ*, 161, 269
- Gao, P., Wakeford, H. R., Moran, S. E., & Parmentier, V. 2021, *J. Geophys. Res. (Planets)*, 126, e06655
- Gasman, D., Min, M., & Chubb, K. L. 2022, *A&A*, 659, A114
- Gordon, I., Rothman, L., Hargreaves, R., et al. 2021, *JQSRT*, 107949
- Guillot, T. 2010, *A&A*, 520, A27
- Guillot, T., Fletcher, L. N., Helled, R., et al. 2022, *Ap&SS*, submitted [arXiv:2205.04100]
- Hellier, C., Anderson, D. R., Collier Cameron, A., et al. 2014, *MNRAS*, 440, 1982
- Helling, Ch., & Woitke, P. 2006, *A&A*, 455, 325
- Helling, Ch., Woitke, P., & Thi, W.-F. 2008, *A&A*, 485, 547
- Helling, Ch., Woitke, P., Rimmer, P. B., et al. 2014, *Life*, 4, 142
- Helling, Ch., Lee, G., Dobbs-Dixon, I., et al. 2016, *MNRAS*, 460, 855
- Helling, Ch., Gourbin, P., Woitke, P., & Parmentier, V. 2019a, *A&A*, 626, A133
- Helling, Ch., Iro, N., Corrales, L., et al. 2019b, *A&A*, 631, A79
- Helling, Ch., Kawashima, Y., Graham, V., et al. 2020, *A&A*, 641, A178
- Helling, Ch., Lewis, D., Samra, D., et al. 2021, *A&A*, 649, A44
- Helling, Ch., Samra, D., Lewis, D., et al. 2022, *A&A*, in press, <https://doi.org/10.1051/0004-6361/202243956>
- Irwin, P. G. J., Parmentier, V., Taylor, J., et al. 2020, *MNRAS*, 493, 106
- Kataria, T., Showman, A. P., Lewis, N. K., et al. 2013, *ApJ*, 767, 76
- Khorshid, N., Min, M., Désert, J. M., Woitke, P., & Dominik, C. 2021, *A&A*, 667, A147
- Kramida, A., Ralchenko, Y., & Reader, J. 2013, *NIST Atomic Spectra Database – Version 5*, <http://www.nist.gov/pml/data/asd.cfm>
- Kreidberg, L., Bean, J. L., Désert, J.-M., et al. 2014, *ApJ*, 793, L27
- Lee, E., Helling, Ch., Dobbs-Dixon, I., & Juncher, D. 2015, *A&A*, 580, A12
- Li, G., Gordon, I. E., Rothman, L. S., et al. 2015, *ApJS*, 216, 15
- Looyenga, H. 1965, *Physica*, 31, 401
- McKemmish, L. K., Yurchenko, S. N., & Tennyson, J. 2016, *MNRAS*, 463, 771
- McKemmish, L. K., Masseron, T., Hoeijmakers, H. J., et al. 2019, *MNRAS*, 488, 2836
- Miles, B. E., Biller, B. A., Patapis, P., et al. 2022, *AAS*, submitted [arXiv:2209.00620v1]
- Min, M., Dominik, C., & Waters, L. B. F. M. 2004, *A&A*, 413, L35
- Min, M., Hovenier, J. W., & de Koter, A. 2005, *A&A*, 432, 909
- Min, M., Ormel, C. W., Chubb, K., Helling, Ch., & Kawashima, Y. 2020, *A&A*, 642, A28
- Molaverdikhani, K., Helling, Ch., Lew, B. W. P., et al. 2020, *A&A*, 635, A31
- Nikolov, N., Sing, D. K., Fortney, J. J., et al. 2018, *Nature*, 557, 526
- Nikolov, N. K., Sing, D. K., Spake, J. J., et al. 2022, *MNRAS*, 515, 3037
- Öberg, K. I., & Bergin, E. A. 2016, *ApJ*, 831, L19
- Ohno, K., Okuzumi, S., & Tazaki, R. 2020, *ApJ*, 891, 131
- Ormel, C. W., & Min, M. 2019, *A&A*, 622, A121
- Patrascu, A. T., Tennyson, J., & Yurchenko, S. N. 2015, *MNRAS*, 449, 3613
- Polyansky, O. L., Kyuberis, A. A., Zobov, N. F., et al. 2018, *MNRAS*, 480, 2597
- Pontoppidan, K., Blome, C., Braun, H., et al. 2022, *ApJL*, 936, L14
- Rigby, J., Perrin, M., McElwain, M., et al. 2022, *PASP*, submitted, [arXiv:2207.05632]
- Robbins-Blanch, N., Kataria, T., Batalha, N. E., & Adams, D. J. 2022, *ApJ*, 930, 93
- Rothman, L. S., Gordon, I. E., Barber, R. J., et al. 2010, *JQSRT*, 111, 2139
- Samra, D., Helling, Ch., & Min, M. 2020, *A&A*, 639, A107
- Samra, D., Helling, Ch., & Birnstiel, T. 2022, *A&A*, 663, A47
- Schneider, A. D., & Bitsch, B. 2021, *A&A*, 654, A71
- Schneider, A. D., Carone, L., Decin, L., et al. 2022, *A&A*, 664, A56
- Schwartz, J. C., & Cowan, N. B. 2015, *MNRAS*, 449, 4192
- Sousa-Silva, C., Al-Refaie, A. F., Tennyson, J., & Yurchenko, S. N. 2015, *MNRAS*, 446, 2337
- Tennyson, J., Yurchenko, S. N., Al-Refaie, A. F., et al. 2016, *J. Mol. Spectrosc.*, 327, 73
- Tennyson, J., Yurchenko, S. N., Al-Refaie, A. F., et al. 2020, *JQSRT*, 255, 107228
- Teske, J. K., Thorngren, D., Fortney, J. J., Hinkel, N., & Brewer, J. M. 2019, *AJ*, 158, 239
- Woitke, P., & Helling, Ch. 2003, *A&A*, 399, 297
- Woitke, P., Min, M., Pinte, C., et al. 2016, *A&A*, 586, A103
- Woitke, P., Helling, Ch., Hunter, G. H., et al. 2018, *A&A*, 614, A1
- Yip, K. H., Changeat, Q., Edwards, B., et al. 2020a, *AJ*, 161, 4
- Yip, K. H., Tsiaras, A., Waldmann, I. P., & Tinetti, G. 2020b, *AJ*, 160, 171
- Yousefi, M., Bernath, P. F., Hodges, J., & Masseron, T. 2018, *JQSRT*, 217, 416
- Yurchenko, S. N., Amundsen, D. S., Tennyson, J., & Waldmann, I. P. 2017, *A&A*, 605, A95
- Yurchenko, S. N., Mellor, T. M., Freedman, R. S., & Tennyson, J. 2020, *MNRAS*, 496, 5282
- Yurchenko, S. N., Tennyson, J., Syme, A.-M., et al. 2021, *MNRAS*, 510, 903

Appendix A: GCM parameters

Table A.1: Model parameters for the GCM we used to produce 1D profiles for WASP-96b

Parameter	Value
Dynamical time-step Δt	25 s
Radiative time-step Δt_{rad}	100 s
Stellar Temperature ¹ (T_*)	5540 K
Stellar Radius ¹ (R_*)	1.05 R_{sun}
Semi-major axis ¹ (a_p)	0.0453 au
Substellar irradiation temperature ² (T_{irr})	1819 K
Planetary Radius ¹ (R_p)	1.2 R_{Jup}
Specific heat capacity at constant pressure ³ (c_p)	13784 J kg ⁻¹ K ⁻¹
Specific gas constant ³ (R)	3707 J kg ⁻¹ K ⁻¹
Rotation period (P_{rot})	3.4 days
Surface gravity (g)	826 cm s ⁻²
Lowest pressure (p_{top})	10 ⁻⁵ bar
Highest pressure (p_{bottom})	700 bar
Vertical Resolution (N_{layers})	47
Wavelength Resolution ⁴ ($S1$)	11

Notes: 1. Values taken from Hellier et al. (2014), 2. Calculated using Eq. (1) from (Guillot 2010), 3. Inferred using the petitRADTRANS equilibrium package, 4. Same as Kataria et al. (2013), benchmarked in Appendix B. of Schneider et al. (2022)

Appendix B: Posterior distributions

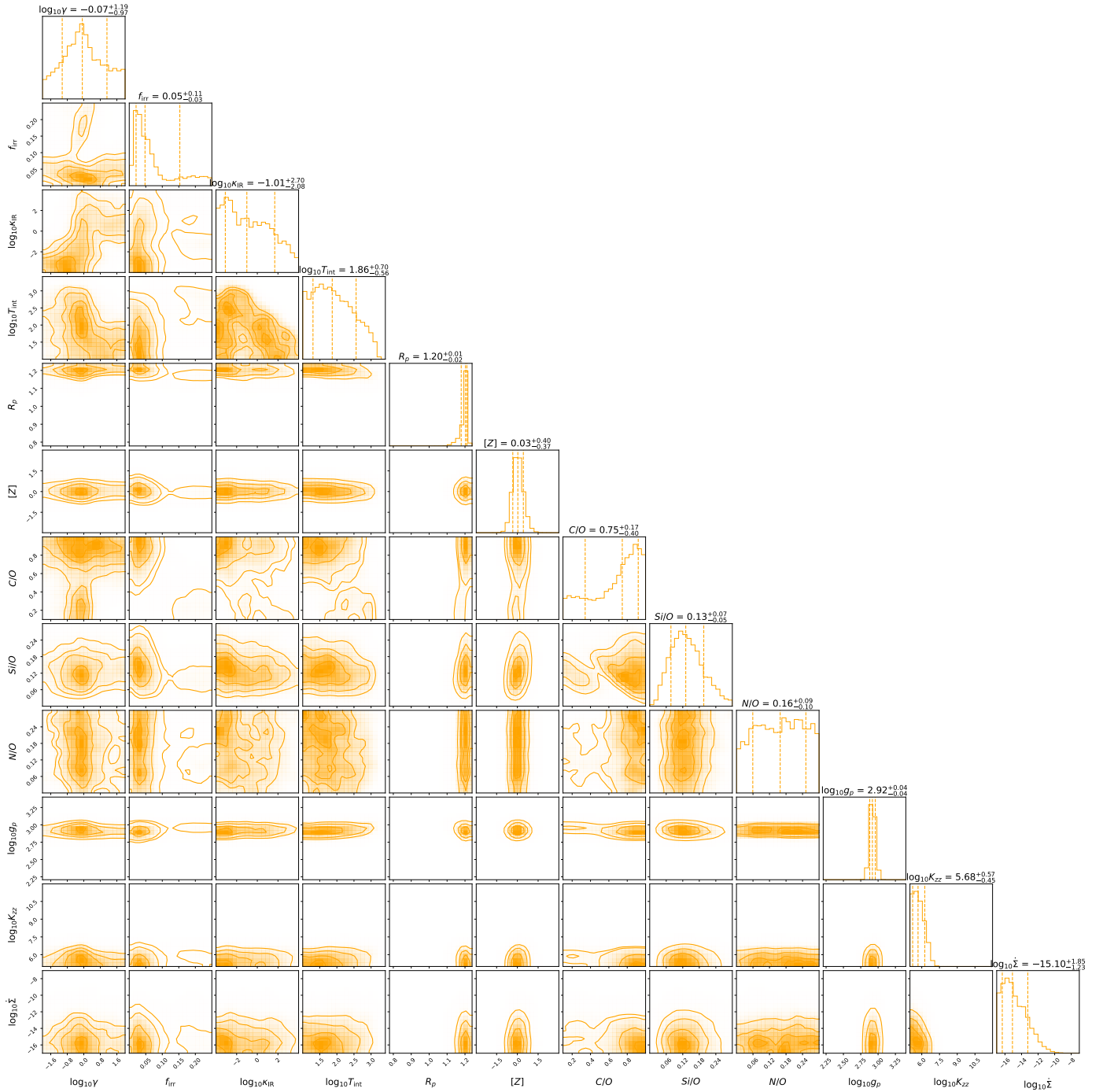


Fig. B.1: Posterior distributions for the equilibrium chemistry retrieval of Nikolov et al. (2022) pre-JWST observations with cloud formation (as described in Ormel & Min (2019)). See Fig. 6 (right) for the pressure–temperature profile, which was computed using retrieved parameters for a pressure–temperature profile based on that of Guillot (2010). All parameters are described in Table 1.

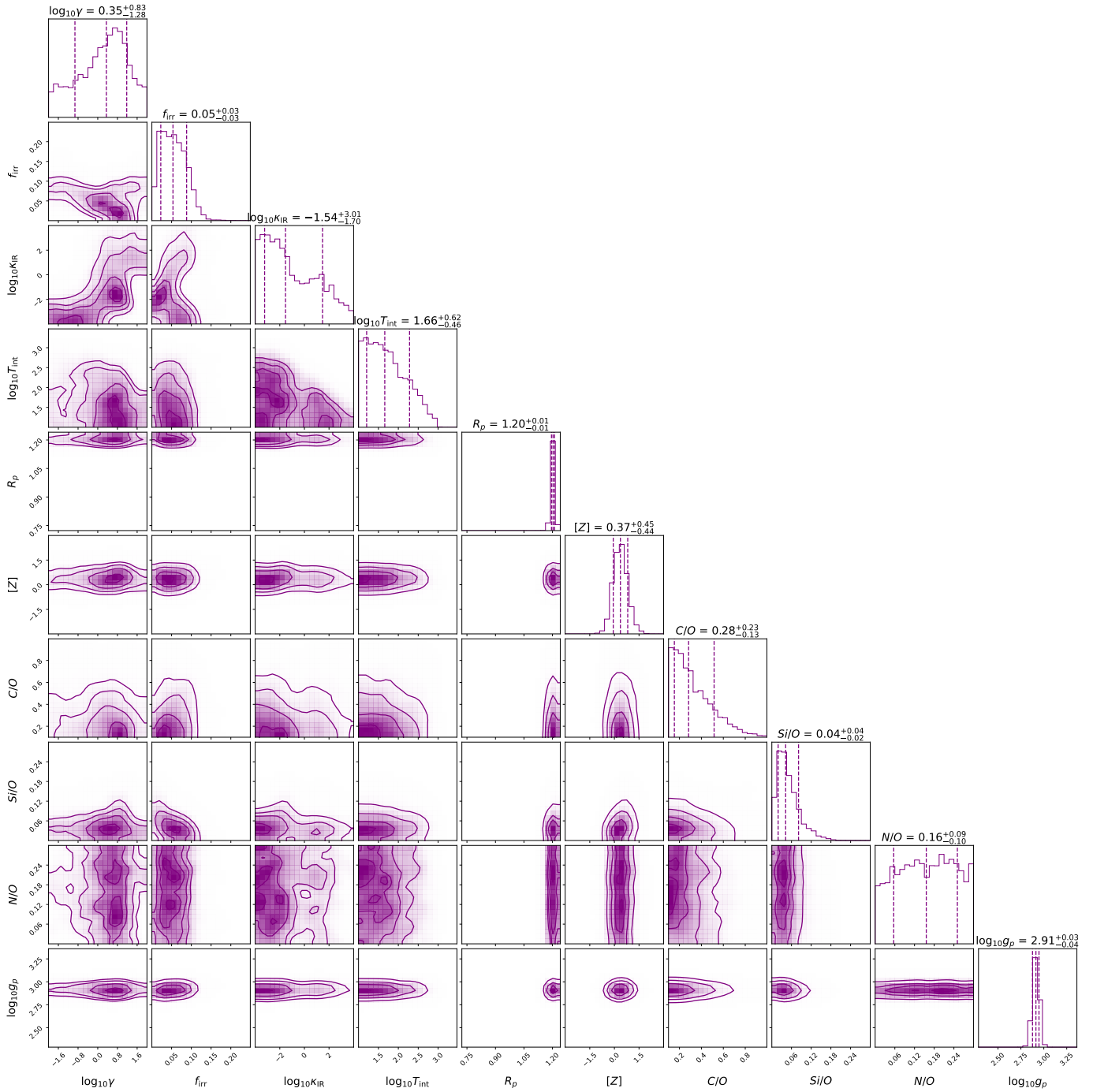


Fig. B.2: Posterior distributions for the equilibrium chemistry retrieval of Nikolov et al. (2022) pre-JWST observations without cloud parameters.

Appendix C: Additional retrieval figures

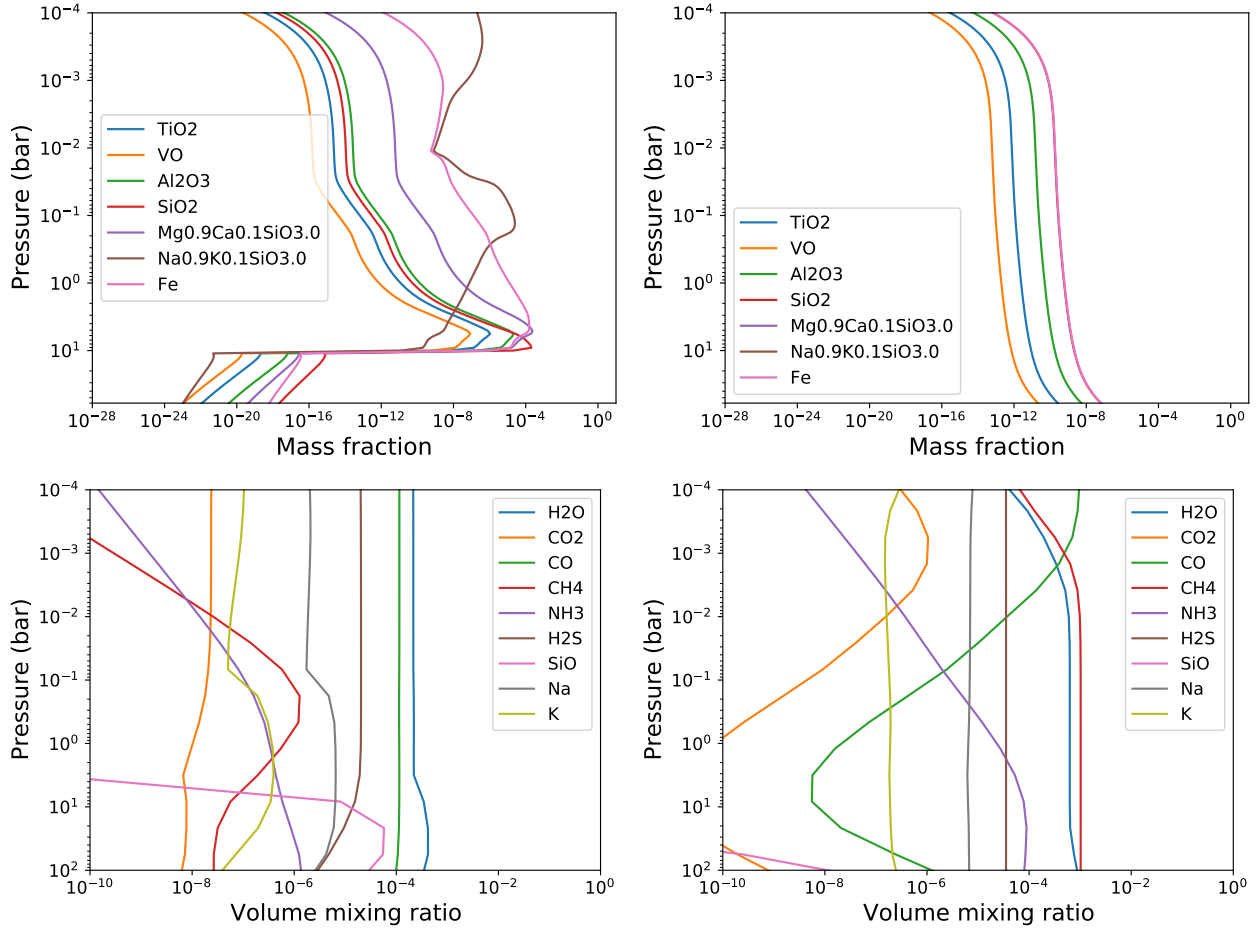


Fig. C.1: Retrieved mass fractions (solid mass / gas mass) for the main cloud species that formed in the constrained cloud formation retrievals (top), and the corresponding volume mixing ratios of the most abundant molecular species included in the retrievals (bottom). **Left:** Best-fit solution ($C/O = 0.15$, higher temperature). **Right:** MPM solution ($C/O = 0.78$, lower temperature). Cloud species included in the formation models that do not form in high enough amounts to be shown in these plots are H_2O ice, amorphous carbon, and SiC .

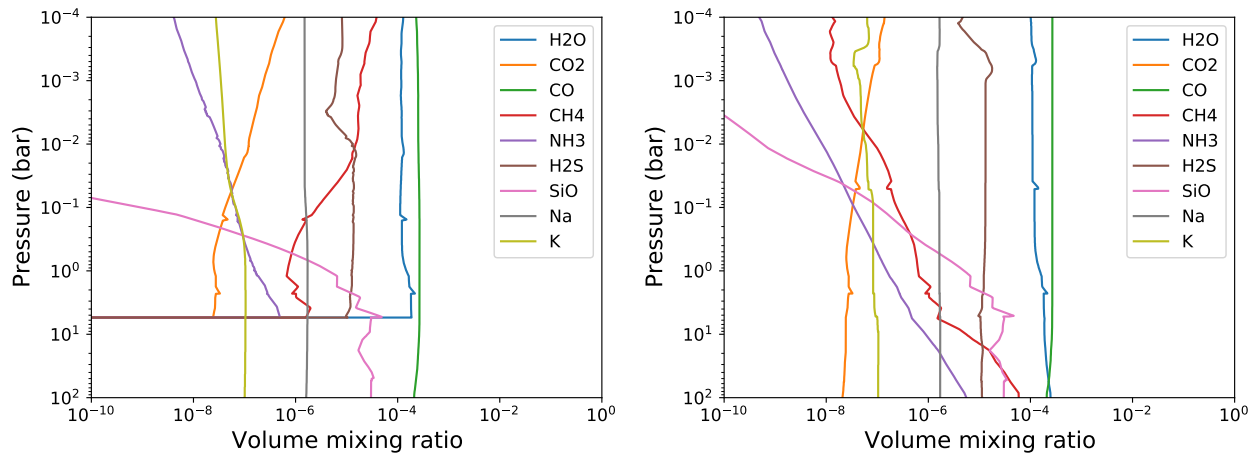


Fig. C.2: Mixing ratios of a selection of the most abundant molecules at the equator of the morning (left) and evening (right) terminator predicted by the GCM and cloud formation models of this work.